Advanced Energy Materials

ADVANCED ENERGY MATERIALS
www.advenergymat.de

RESEARCH ARTICLE OPEN ACCESS

Ultrathin Aluminum–Air Batteries via Hygroscopic Electrolytes for Continuous Operation of Imperceptible On-Skin Electronics

Jaeil Park[1] | Inho Lee[2] | Namhee Kim[1] | Wonseok Shin[1] | Joo Sung Kim[3] | Daegun Kim[4] | Giwon Lee[5] | Jinhan Cho[6] | Hoon-Hee Ryu[7] | Myung-Han Yoon[8] | Seung Joon Yoo[8] | Woo-Jin Song[7,9] | Sungjun Park[1,2]

[1]Department of Electrical and Computer Engineering, Ajou University, Suwon, Republic of Korea | [2]Department of Intelligence Semiconductor Engineering, Ajou University, Suwon, Republic of Korea | [3]Thin-Film Device Laboratory, RIKEN, Wako, Saitama, Japan | [4]School of Chemical, Biological, and Battery Engineering, Gachon University, Seongnam, Republic of Korea | [5]Department of Chemical Engineering, Kwangwoon University, Seoul, Republic of Korea | [6]School of Chemical and Biomolecular Engineering, Korea University, Seoul, Republic of Korea | [7]Department of Chemical Engineering and Applied Chemistry, Chungnam National University, Daejeon, Republic of Korea | [8]Department of Materials Science and Engineering, Gwangju Institute of Science and Technology, Gwangju, Republic of Korea | [9]Institute of Carbon Fusion Technology (InCFT), Chungnam National University, Daejeon, Republic of Korea

Correspondence: Seung Joon Yoo (sjoonyoo@gist.ac.kr) | Woo-Jin Song (wjsong@cnu.ac.kr) | Sungjun Park (sj0223park@ajou.ac.kr)

Received: 25 April 2026 | **Revised:** 2 June 2026 | **Accepted:** 8 June 2026

Keywords: aluminum-corrosion suppression | hygroscopic hydrogel electrolytes | on-skin batteries | self-hydration | skin-conformal biosensors

ABSTRACT

On-skin power sources require ultrathin form factors, safety, and mechanical robustness, but few battery platforms simultaneously satisfy these requirements. Here, we report the thinnest Al–air batteries to date (<270 μm) enabled by hygroscopic hydrogel electrolytes. Operating in a water-in-salt regime with highly concentrated ionic species, strong ion–water interactions suppress electrolyte dehydration and Al self-corrosion, while enabling high-capacity operation of 2479 mAh g^{-1} at 10 mA cm^{-2} in ultrathin architectures. The cells withstand over 3000 bending cycles at a bending radius of 1 mm and remain functional under severe deformation, including crumpling, cutting, and perforation. Stable operation over more than 1000 cycles of repeated anode replacement suggests an operational lifespan exceeding 8000 h. When integrated with organic electrochemical transistor-based biosensors, the system enables continuous, real-time physiological signal monitoring with a signal fidelity of up to 31.1 dB, providing a viable route toward continuous operation of conformal epidermal electronic systems.

1 | Introduction

Epidermal and wearable electronics are rapidly evolving into thinner, softer, and more skin-like forms, yet no existing power source simultaneously satisfies the ultrathin, safe, and mechanically compliant requirements of on-skin systems [1–5]. Conventional lithium-ion batteries (LIBs) are incompatible with skin-mounted applications, as they are designed for high-energy storage and rely on rigid, flammable components that pose safety risks under mechanical deformation [6, 7]. Furthermore, current wearable devices typically depend on wired external battery packs, which limit user mobility and hinder system integration. Consequently, the development of intrinsically safe, ultrathin, and mechanically compliant on-skin power systems capable of stable operation under dynamic mechanical deformation has become a critical challenge for next-generation conformal electronics [8].

Various ultrathin power systems have been explored for epidermal devices, including energy harvesters (e.g., solar cells

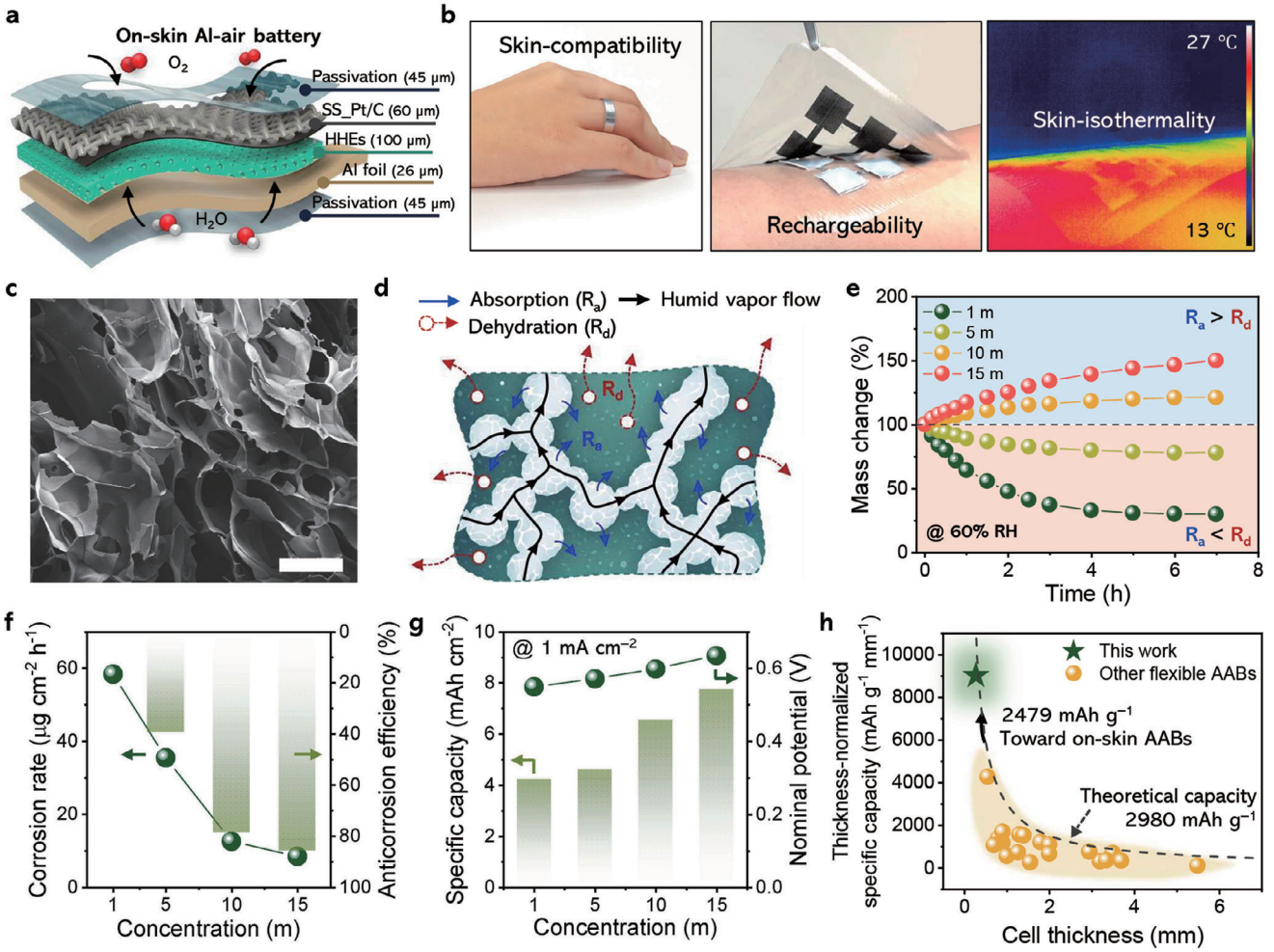

FIGURE 1 | On-skin H-AABs with ultrathin HHEs for powering skin-conformal electronics. (a) Schematic illustration of flexible ultrathin H-AABs comprising SS314 GDL with Pt/C catalyst, HHEs, and Al anode. (b) Wearable ring- type H-AABs and optical and thermographic images of on-skin H-AAB. (c) SEM image of cross-sectional HHEs. Scale bar denotes 200 μm. (d) Illustration of hydration kinetics property of HHEs. (e) Time-dependent mass-change profile of as-prepared HHEs under air at 60% RH. (f) Corrosion rate and anticorrosion efficiency of Al anode on HHE surface. (g) Concentration-dependent specific discharge capacity and nominal potential of on-skin H-AABs under air at 60% RH and 1 mA cm^{-2}. (h) Comparative analysis of thickness normalized specific capacities for hydrogel-based flexible AABs. The dashed line represents the theoretical limit (2980 mAh g^{-1}), providing a benchmark for evaluating the discharge performance of the AABs.

[9], triboelectric generators [10], and thermoelectric generators [11] and metal–air batteries (MABs) [12]. Although energy harvesters convert environmental stimuli into electricity, their output is intermittent and environment-dependent, limiting the continuous operation of electronics [13–15]. Therefore, epidermal systems require alternative power sources that provide stable and sustainable energy delivery under diverse environmental and mechanical deformations for reliable device performance. Among MABs, Li–air systems exhibit the highest theoretical capacity and a discharge potential (~3.0 V) comparable to conventional LIBs [16, 17]. However, their reliance on highly reactive lithium metal and flammable organic electrolytes poses unacceptable safety risks for skin-mounted applications [18]. In contrast, Al–air batteries (AABs) offer a unique combination of high theoretical specific capacity (~2980 mAh g^{-1}), intrinsic safety via aqueous electrolytes, and the use of earth-abundant Al, establishing them as a scalable and robust solution for on-skin power systems [19, 20].

However, translating the advantages of AABs into ultrathin epidermal devices remains challenging. Epidermal power sources require thin and compliant form factors for skin conformability, but reducing battery thickness inevitably limits the electrolyte volume and internal water reservoir. In aqueous AABs, this volumetric constraint accelerates electrolyte dehydration, weakens water retention, and increases parasitic Al corrosion, leading to degraded discharge capacity, ionic conduction, oxygen reduction reaction (ORR) kinetics, and Al utilization [21, 22]. Existing strategies to mitigate dehydration, including glycerol or ionic liquid incorporation, rely on thicker (>500 μm) electrolytes, compromising flexibility [23–26]. Similarly, anticorrosion approaches, including physical barriers and corrosion inhibitors, increase interfacial resistance and fail under repeated mechanical deformation [27, 28]. Therefore, achieving simultaneous water retention and corrosion suppression in ultrathin AABs remains a critical challenge.

Here, we demonstrate ultrathin AABs with a total thickness below 270 μm, overcoming the long-standing trade-off between thickness and capacity of AABs. Hygroscopic hydrogel electrolytes (HHEs) operating in a water-in-salt regime suppress water activity through strong ion–water interactions while retaining sufficient hydration by absorbing moisture from the air, enabling sustained ORR kinetics while limiting Al anode corrosion in ultrathin architectures and delivering a near-theoretical specific capacity of 2479 mAh g^{-1} at 10 mA cm^{-2}. The devices withstand over 3000 bending cycles at a radius of 1 mm and remain functional under extreme mechanical deformation, including crumpling, cutting, and perforation. Repeated Al anode replacement supports stable operation over more than 1000 cycles, corresponding to an operational lifespan exceeding 8000 h. Integration with organic electrochemical transistor-based biosensors enables continuous physiological signal monitoring with a signal fidelity of up to 31.1 dB.

2 | Results and Discussions

2.1 | Design and Electrical Performance of Ultrathin On-Skin H-AABs

To achieve an on-skin hygroscopic AAB (H-AAB), we integrated a 50 μm-thick stainless-steel (SS) mesh-based gas diffusion layer (GDL) with a 10 μm-thick Pt/C catalyst layer, a 100 μm-thick HHE (Figure S1), a 26 μm-thick Al foil, and two 45 μm-thick passivation layers (Tegaderm) (Figure 1a). The active H-AAB stack had a thickness of approximately 180 μm. After encapsulation with top and bottom passivation layers, the fully encapsulated on-skin H-AAB exhibited a total device thickness of approximately 270 μm. Unlike conventional carbon cloth-based GDLs (>250 μm) that are typically bulky, ultrathin plain-weave SS mesh offers a silk-like texture and superior mechanical resilience. By leveraging the intrinsic ductility of the metallic framework, the SS mesh maintains its structural integrity and high porosity even after catalyst coating (Figure S2). The H-AAB demonstrates exceptional imperceptible skin compatibility in both ring-type and on-skin formats, while its mechanically rechargeable design allows for sustainable power. Furthermore, thermographic analysis confirms a stable operating temperature consistent with human skin (near 20°C–25°C), ensuring thermal safety and wearer comfort for long-term epidermal applications (Figure 1b).

The HHEs were synthesized from a poly(acrylic acid–co-acrylamide) matrix to enable continuous water replenishment (Figure S3) [29]. Successful polymerization was verified by the complete disappearance of the characteristic C═C─H peaks at 976 cm^{-1} for acrylic acid and 956 cm^{-1} for acrylamide in FT-IR spectra (Figure S4) [30]. The HHE cross-sectional SEM image reveals a microporous structure that facilitates the effective transport of water vapor (Figure 1c) [31]. Hydration kinetics are governed by the equilibrium between dehydration (R_d]. and moisture absorption rate (R_a) (Figure 1d); the hydrogel progressively shrinks when $R_d > R_a$, whereas it swells via atmospheric moisture uptake when $R_d \leq R_a$. Under 60% relative humidity (RH) (Figure 1e), low-salt-concentration HHEs (1 and 5 m) exhibit significant mass reduction, while the 10 and 15 m HHEs show spontaneous swelling with mass gains of 21% and 51% after 7 h, respectively. This hygroscopicity is highly sensitive to ambient humidity, with the 15 m HHE showing mass increases of 21%, 51%, and 102% at 40%, 60%, and 80% RH (Figure S5). High-concentration HHEs maintain stable ionic conductivity over time, whereas the 1 m HHE exhibits a continuous decline (Figure S6 and Table S1). Furthermore, the HHE stabilizes the Al anode by suppressing self-corrosion. The corrosion rate dropped from 58.3 μg cm^{-2} h^{-1} for the 1 m HHE to 8.3 μg cm^{-2} h^{-1} for the 15 m HHE (Figure 1f), representing an anticorrosive efficiency of 85.7% (Figure S7). Al corrosion is both thermodynamically and kinetically suppressed in highly concentrated HHEs, as evidenced by the positive shift in corrosion potential and the reduction in current density (Figure S8 and Table S2).

Driven by these enhanced hydration and anticorrosive properties, H-AAB with 100-μm-thick 15 m HHEs exhibited areal capacities of 7.8 mAh cm^{-2} at 1 mA cm^{-2}, outperforming existing flexible AABs (Figure 1g, Figure S9). For instance, AABs using 150-μm-thick membrane/NaCl, 75-μm-thick PVA/Gly/NaCl, and 300-μm-thick PVA/PEO/LiCl hydrogels exhibited areal capacities of 6.7, 1.3, and 0.6 mAh cm^{-2} at 1 mA cm^{-2}, respectively [21, 32, 33]. Notably, the 15 m H-AAB achieved a maximum gravimetric specific capacity of 2479 mAh g^{-1} at 10 mA cm^{-2} (Figure S10), approaching the theoretical limit of Al utilization. To enable direct comparison with existing wearable batteries, we introduce thickness-normalized specific capacity as a key performance metric (Figure 1h). This hygroscopic, ultrathin design harvests ambient moisture to supply power, eliminating the need for bulky packaging or external water reservoirs. The resulting structural and chemical synergy provides a low-profile, high-capacity energy source for reliable operation on skin.

2.2 | Water Confinement–Mediated Anticorrosion and High-Capacity Operation

The superior discharge characteristics of 15 m H-AABs stem from suppression of water activity within the highly concentrated HHE, which mitigates severe self-corrosion [34]. This effect arises from the high LiCl concentration, which reinforces the hydrogen-bonding network and restricts water activity, thereby increasing the activation energy barrier for parasitic water reduction [35]. At low concentrations (1 m), water molecules predominantly exist as free water or within the outer solvation shells of ions (Figure 2a,i). In contrast, the high-concentration HHE exhibits a reduced water-to-ion molar ratio of 1.8 (compared to 27.8 for 1 m), effectively confining most water molecules to strong ion-solvation states or hydrogen bonding with the polymer matrix (Figure 2a-ii, Table S3) [36]. This transition is supported by differential scanning calorimetry (Figure 2b,c), where the distinct melting peak at −4°C and −33°C observed for the 1 and 5 m HHE disappears entirely above 10 m (Figure S11). The absence of phase-transition peaks indicates that restricted molecular mobility in highly concentrated HHEs suppresses ice crystallization even at −100°C [37]. Furthermore, Raman spectroscopy (Figure 2d) shows a pronounced decrease in the intensities of νOH_{free} (3580 cm^{-1}) and νOH_{Sym} (3262 cm^{-1}) with increasing LiCl concentration. Notably, the νOH_{Asym} (3441 cm^{-1}) configuration, associated with strong ion-hydration shells, increases to 84.5% in the 15 m HHE, while free water is reduced to 0.8% (Figure 2e, Figure S12), indicating that the activity of confined water is restricted within the solvation shells [38, 39].

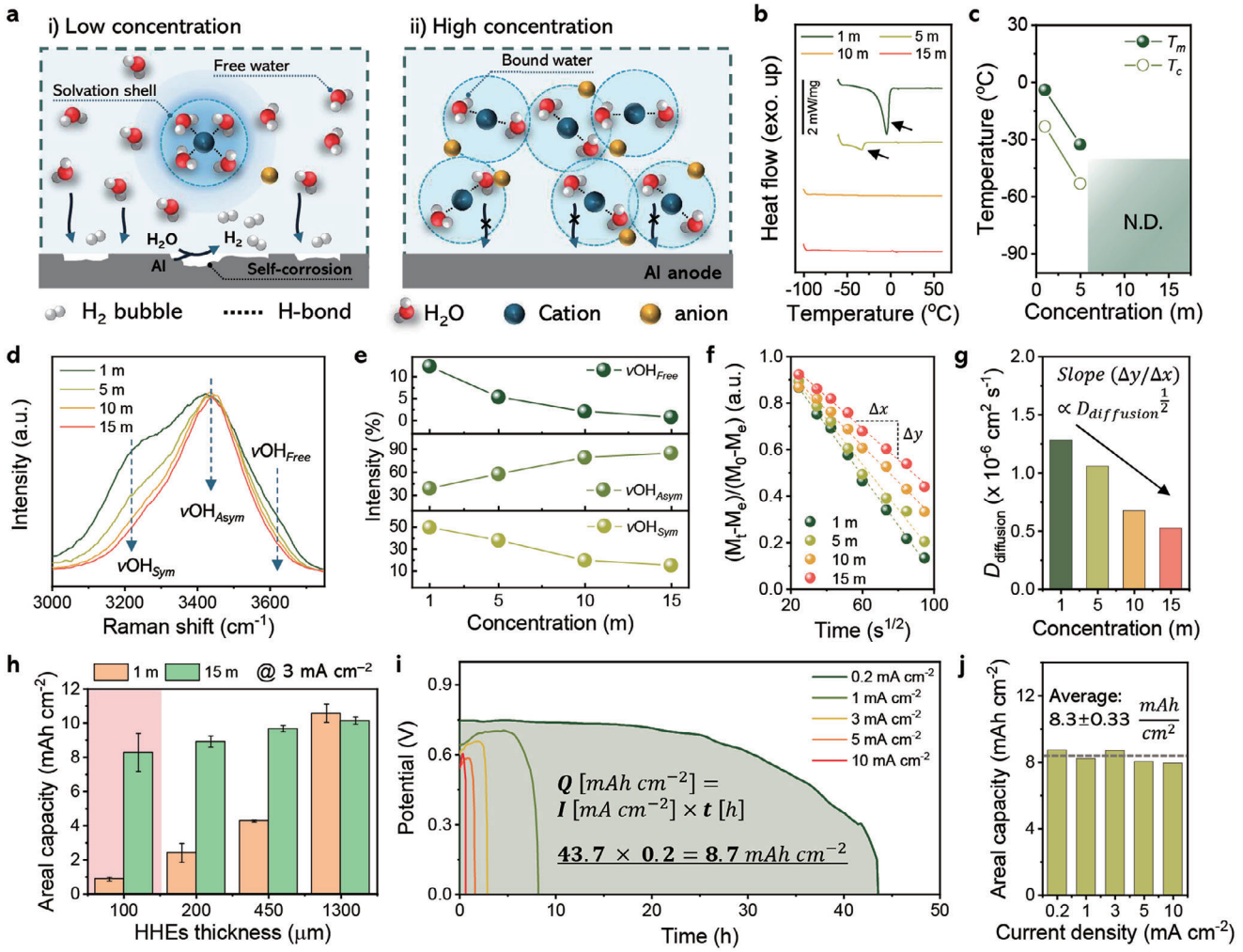

FIGURE 2 | Physicochemical environments of water in highly concentrated HHEs. (a) Schematic illustration of intermolecular interaction of (i) low- and (ii) high- concentration HHEs. (b) DSC heating curves of HHEs. Arrows point to melting peak of HHEs. (c) Melting (T_m) and crystallization (T_c) temperature of HHEs. T_m and T_c peaks of 10 and 15 m HHEs were not detected. (d) Magnified Raman spectra of 1, 5, 10, and 15 m HHEs in the range from 3000 to 4000 cm^{-1}. (e) Intensity of various –OH bond configurations by deconvoluting Raman peak ranging from 3000 to 4000 cm^{-1}. (f) Concentration-dependent diffusion model of water molecules in HHEs pores under 60% RH. Linear fitting is shown by dashed line. (g) Calculated diffusion coefficients from slope of linear fit. (h) HHE thickness-dependent areal capacity of 1 and 15 m H-AABs at a current density of 3 mA cm^{-2}. (i) Discharge profile of 15 m H-AABs at a current density of 0.2–10 mA cm^{-2} under air at 60% RH. (j) Current-dependent specific discharge capacity of 15 m H-AABs under air at 60% RH.

The diffusion behavior of water molecules, quantified using Fick's second law under non-steady-state conditions (Figure 2f), reflects this constrained environment [40, 41]. The calculated diffusion coefficient ($D_{diffusion}$) decreased gradually from 1.27, 1.05, 0.67, and 0.52 × 10^{-6} cm^2 s^{-1} for the 1, 5, 10, and 15 m HHEs at 60% RH (Figure 2g). Interestingly, $D_{diffusion}$ for all HHEs remained nearly constant regardless of atmospheric RH (Figure S13). Impedance analysis corroborates these sluggish kinetics, showing a diffusion-limited response in the low-frequency region at high salt concentrations in the HHE (Figure S14). This reduced diffusivity limits water transport to the electrode interface, increasing the activation energy for water reduction and thereby suppressing parasitic reactions, effectively passivating the Al anode and enabling high specific capacities.

The practical impact of these concentrated HHEs is most evident in the thickness-dependent performance of the H-AAB. The discharge capacity of 1 m H-AABs is severely limited by rapid dehydration and limited water availability, yielding an areal capacity of only 1.0 mAh cm^{-2} with 100 μm-thick HHE (Figure 2h). In sharp contrast, the 15 m H-AAB maintains a high areal capacity of 8.3 mAh cm^{-2} even at 100 μm thickness, demonstrating the effectiveness of the hygroscopic and anticorrosive design in sustaining electrochemical activity under water-limited conditions. As the HHE thickness increases to 1300 μm, the capacities of the two systems converge, as the larger water reservoir in the 1 m HHE eventually mitigates dehydration. Long-term operational stability and low self-discharge are critical for wearable power sources. In on/off cycling tests at 0.5 mA cm^{-2}, the 1 m H-AAB fails after only 14 h due to severe Al self-corrosion during off-periods and electrolyte dry-out (Figure S15a). By contrast, the 15 m H-AAB sustains operation for approximately 27 h, enabled by enhanced anticorrosion properties and intrinsic hygroscopic water-retention capability (Figure S15b).

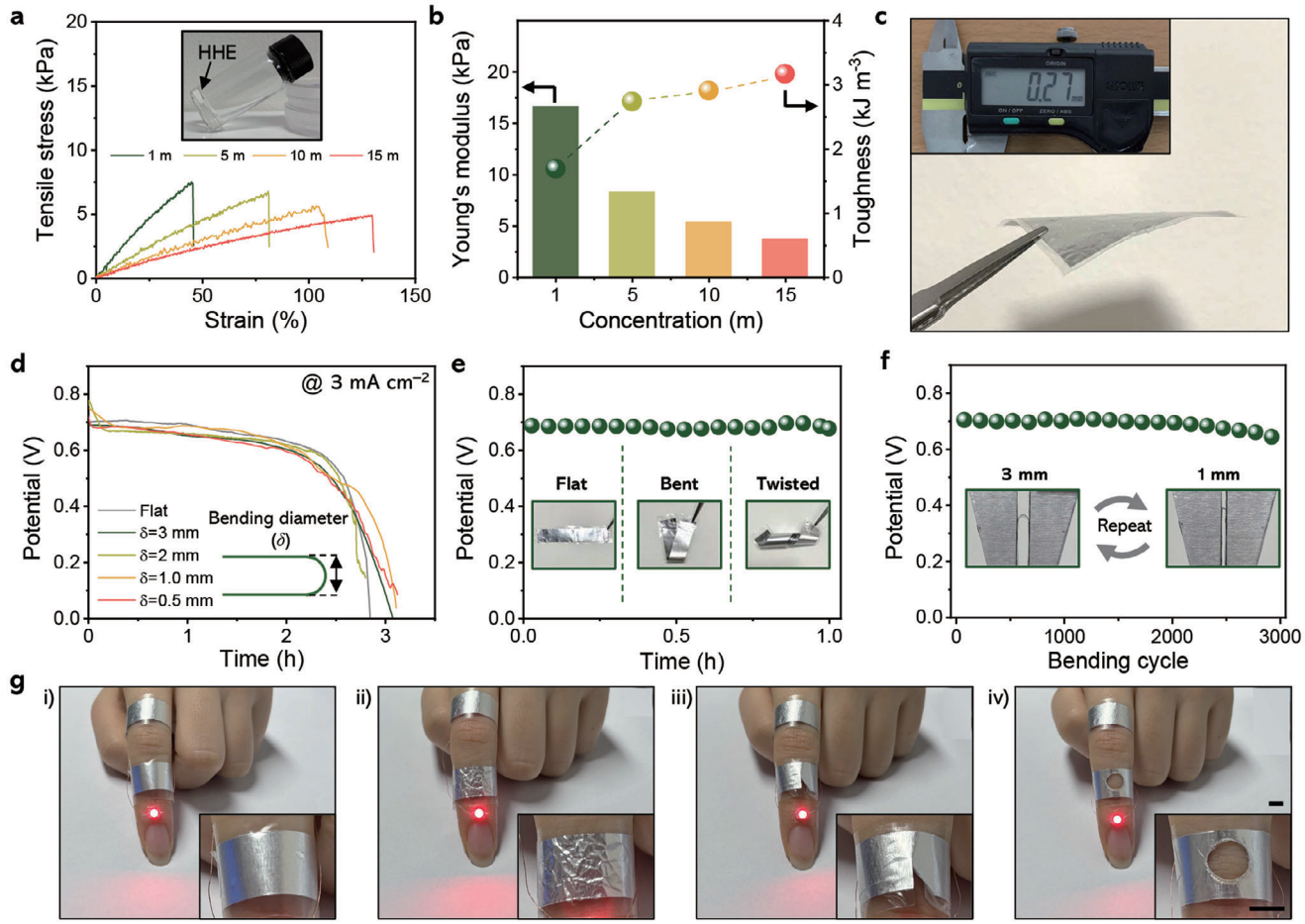

FIGURE 3 | Mechanical properties and safety of ultrathin H-AABs. (a) Strain–stress curves of HHEs. Inset image shows HHE synthesized in a vial. (b) Concentration-dependent Young's modulus and toughness of HHEs. (c) Photograph of the fabricated H-AAB. The thickness of the fully encapsulated H-AAB, including top and bottom passivation layers, was measured using a vernier caliper. (d) Discharge profiles of H-AABs at various bending diameter ranging from 3.0 to 0.5 mm at 3 mA cm^{-2}. Dimension of H-AABs for flexibility test was 2×11 cm^2. (e) Discharge behaviors of ultrathin 15 m H-AABs under flat, bent, and twisted states at 0.5 mA cm^{-2}. (f) Discharge profile in repeated bending/released cycles at bending diameter of 1.0 mm at 0.5 mA cm^{-2}. (g) Stability and safety evaluation of series-connected H-AABs, which showed sustained LED illumination at (i) bare, (ii) crumpled, (iii) cut, and (iv) perforated states. Scale bars denote 5 mm.

The 15 m H-AAB achieved 43.6 h of continuous discharge operation at 0.2 mA cm^{-2} (Figure 2i). Across a wide range of current densities (0.2–10 mA cm^{-2}), the 15 m H-AAB consistently maintains an areal capacity of between 8.0 and 8.7 mAh cm^{-2} (Figure 2j), underscoring its potential for reliable on-skin epidermal power sources.

2.3 | Mechanically Resilient and Damage-Tolerant Ultrathin H-AABs

The transition in ion–water–polymer interactions within the HHE governs both electrochemical stability and the mechanical constitutive behavior of the electrolyte. Stress–strain analysis reveals that the 1 m HHE exhibits a tensile strain of 45% and a tensile strength of 7.5 kPa, reflecting a relatively stiff and brittle nature (Figure 3a). In contrast, the 15 m HHE achieves a tensile strain of 131% with a tensile strength of 5 kPa, indicating substantially enhanced mechanical compliance. This transition arises from the interplay between polymer plasticization and dynamic hydrogen bonding at high salt concentrations. The pristine hydrogel is brittle due to dominant chemical crosslinking, whereas concentrated electrolytes plasticize the polymer matrix while simultaneously forming a dense network of reversible hydrogen bonds. These combined effects soften the matrix while promoting energy dissipation under deformation. As a result, the Young's modulus decreases to 3.7 kPa, and the toughness nearly doubles to 3.3 kJ m^{-3} (Figure 3b). The resulting modulus closely matches that of human epidermis, enabling conformal contact with skin without interlayer delamination or irritation [42, 43].

The resulting H-AAB, with a total thickness of 0.27 mm including passivation layers (Figure 3c), enables conformal integration with the complex topography of human skin without mechanical constraint. Mechanical robustness was evaluated through discharge tests under extreme bending conditions, with bending diameters (δ) down to 0.5 mm (Figure 3d). Given the device thickness of 0.27 mm, such deformation imposes out-of-plane compressive strain across the multilayer structure rather than simple flexural bending. Despite these conditions, the 15 m H-AAB maintains stable electrochemical operation, indicating

that the HHE matrix effectively accommodates localized strain while preserving structural integrity. This behavior arises from the viscoelastic nature of the concentrated HHE, in which dynamic hydrogen-bond networks dissipate mechanical energy and prevent crack propagation. As a result, gas diffusion pathways and ionic conduction channels remain uninterrupted even under extreme deformation. At a current density of 0.5 mA cm^{-2}, the device delivers a stable discharge potential of 0.68 V across flat, bent, and twisted configurations (Figure 3e), demonstrating that electrochemical performance is decoupled from macroscopic deformation. This mechanical invariance is further supported by strong interfacial adhesion between the compliant HHE and the electrodes, which suppresses interfacial delamination and maintains ion-transport pathways during repeated deformation. Durability was demonstrated over 3000 bending–release cycles at $\delta = 1.0$ mm (Figure 3f), with no observable potential decay or interfacial degradation, indicating stable electrochemical operation under repeated mechanical strain and suitability for integration with skin-compatible electronics.

Beyond individual cell reliability, we demonstrate the system-level damage tolerance and stable operation of H-AAB assemblies under selected mechanical damage conditions. A ring-type H-AAB continues to power a light-emitting diode under severe deformation, including high-density crumpling, cutting, and perforation (Figure 3g,i–iv), conditions that exceed the mechanical strain encountered during typical human motion or textile deformation. The sustained operation under these conditions indicates that electrochemical functionality is preserved despite structural discontinuities, reflecting the tolerance of the system to localized mechanical damage. This damage tolerance arises from the non-flammable aqueous HHE, which suppress uncontrolled reactions even under mechanical failure or internal short-circuiting. In contrast to conventional lithium-ion batteries prone to thermal runaway upon structural damage, the H-AAB maintains stable operation without thermal or electrochemical instability, indicating that electrochemical functionality is effectively decoupled from mechanical integrity even under severe deformation.

2.4 | System-Level Integration for Continuous On-Skin Bioelectronics

We introduce a mechanical recharge strategy based on physical Al anode replacement. Here, mechanical recharge refers to replacing the consumed Al anode with a fresh Al foil to restore discharge capability, rather than electrochemically recharging the AAB. This mechanically refreshed design supports continuous operation while bypassing the intrinsic rechargeability limitation of conventional primary AAB systems. The flexibility and self-hydrating nature of the HHE allow rapid, skin-interfaced replacement of active components, while periodic electrolyte refreshes maintain a stable electrochemical environment. This approach effectively decouples the total energy capacity from the initial fuel inventory, enabling sustained power delivery for long-term on-skin operation. To evaluate the reversibility and interfacial stability of this process, the cell was subjected to 1000 mechanical recharge cycles (Figure 4a). The cell potential remained stable above 0.7 V throughout cycling, indicating minimal electrochemical degradation despite repeated mechanical handling and interface reconstruction. Based on stable cycling behavior over 1000 mechanical recharge cycles and an average discharge duration of ~8 h per cycle, the projected cumulative operational lifetime exceeds 8000 h. These results indicate that system longevity is governed by mechanical refueling frequency.

Thermal safety, a critical requirement for on-skin electronics, was evaluated during continuous discharge at 1 mA cm^{-2} (Figure 4b). The hydrogel electrolyte buffers the exothermic oxidation of the Al anode through its high latent heat, maintaining the device surface temperature near 25°C even during prolonged operation. This near-ambient temperature profile minimizes the risk of thermal discomfort or skin irritation, ensuring safe operation under direct epidermal contact (Figure S16). The scalability of the H-AAB system was further demonstrated through series and parallel configurations (Figure 4c). Two cells connected in series increased the nominal discharge potential to 1.23 V, while a parallel configuration increased the areal capacity from 8.7 to 19.8 mAh cm^{-2} at 3 mA cm^{-2}. Accordingly, a 2S2P configuration would enable simultaneous enhancement of both voltage and capacity. With an areal power density of 8.3 mW cm^{-2} (Figure S17), the system meets the energy and power requirements for autonomous wearable and skin-conformal electronics.

To demonstrate standalone, integrated operation, the H-AAB-powered skin-conformal system was applied to real-time biosignal monitoring using organic electrochemical transistor (OECT)-based sensors (Figure S18). The mechanical compliance of the H-AAB allows the battery to conform to wrinkle-scale skin deformations during wrist motion while maintaining stable power delivery without delamination (Figure 4d, Figure S19). This low-profile and compliant power source is therefore suitable for imperceptible epidermal electronics, where stable skin contact and minimal mechanical burden are required during natural motion. When the OECT was not in contact with the skin, wrist motion produced a stable baseline despite deformation of the H-AAB (Figure 4e, top), indicating that mechanical deformation of the power source introduces negligible electrical noise. In contrast, with the OECT in contact with the skin, identical motion generated clear variations in the RMS signal corresponding to muscle activation (Figure 4e, bottom). This confirms that the H-AAB provides a mechanically robust, noise-free power source for biosignal acquisition. Under this stable power supply, the RMS current reproducibly varies between 0.4 and 0.9 μA in response to muscle activity. When integrated with an EMG sensor on the forearm, the device resolves force-dependent muscle activity across a 10–40 kg range, with RMS values scaling from 0.8 to 3.3 μA (Figure 4f). Importantly, this stable power delivery enables continuous ECG monitoring in a clinically relevant, chest-mounted configuration (Figure 4g), which conventionally relies on rigid and bulky batteries. The system maintains a consistent signal-to-noise (S/N) ratio of ~30 dB over 1000 mechanical recharge cycles without degradation (Figure 4h). Noise analysis shows a reduction in current noise from 49 μA (commercial source meter) to below 1 μA for the H-AAB (Figure S20). These results demonstrate that the ultrathin H-AAB serves as a reliable power platform for integrated, multimodal skin-conformal bioelectronics.

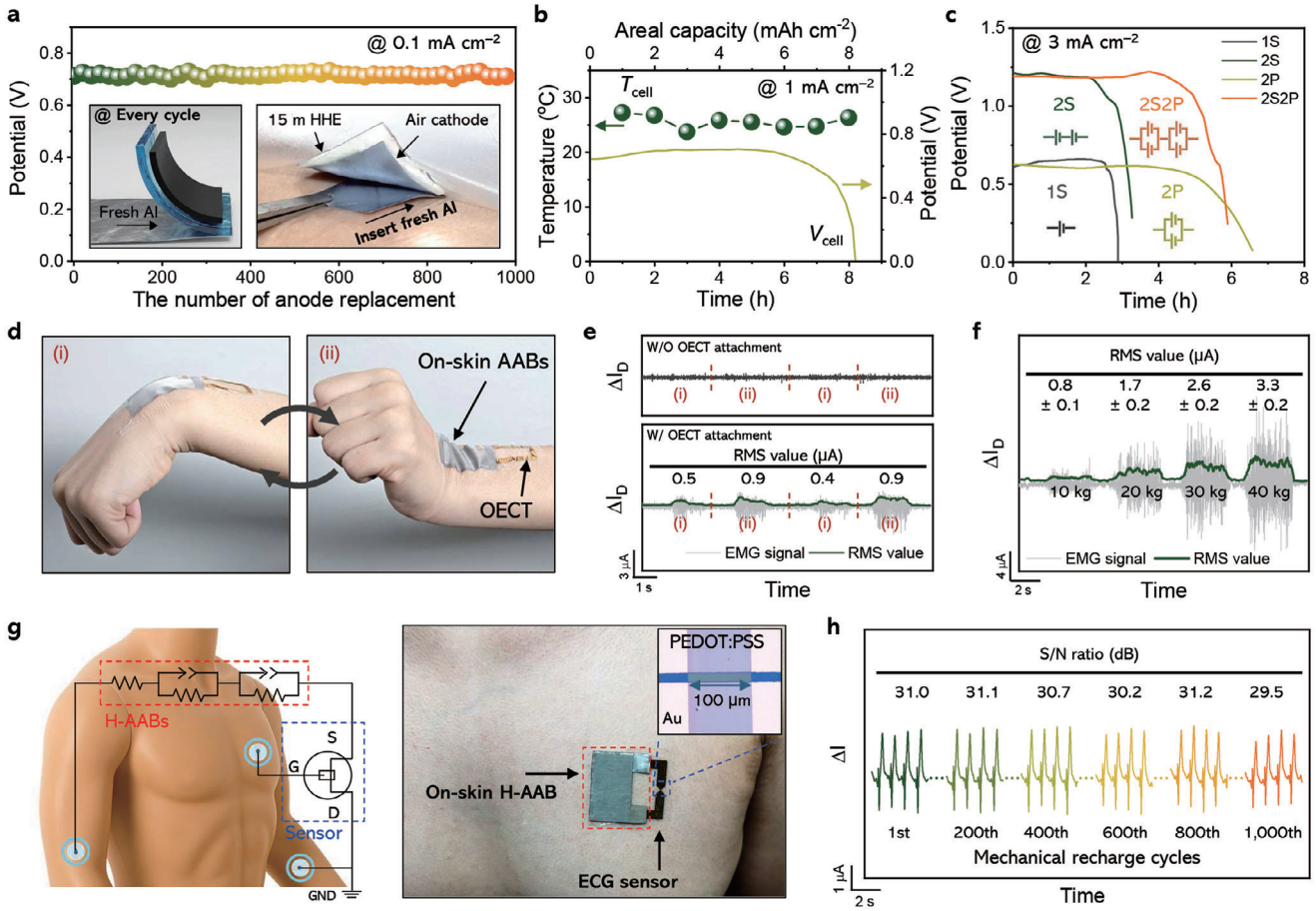

FIGURE 4 | Integrated skin-conformal biosensor systems with on-skin H-AABs. (a) Voltage evolution of 15 m H-AABs upon repeated mechanical recharge by replacing Al anode every cycle at 0.1 mA cm^{-2}. (b) Surface temperature of H-AABs at every 1 h of galvanostatic discharge at 1 mA cm^{-2}. (c) Discharge profiles of series and parallel-connected 15 m HHEs at 3 mA cm^{-2} under 60% RH. (d) Images showing movements of wrist attached with skin-conformal EMG sensor system. (e) EMG-signal measurements during wrist movements. (f) Force-dependent EMG signals recorded by integrated skin-conformal EMG sensor system. (g) Equivalent circuit and photograph of skin-conformal ECG sensor system on chest. Inset shows magnified image of ECG sensor. (h) ECG signals and S/N ratio of integrated ECG sensor system powered by mechanically rechargeable 15 m H-AAB. Signals were recorded every 200 cycles.

3 | Conclusions

In summary, we report an ultrathin (~270 μm), mechanically compliant on-skin AAB platform for imperceptible epidermal electronics, which overcomes the persistent challenges of dehydration and Al corrosion in flexible MABs. By engineering a highly concentrated LiCl-based hydrogel electrolyte, we enable autonomous atmospheric moisture harvesting and suppress water activity at the molecular level, thereby inhibiting parasitic reactions. The resulting H-AAB delivers a high specific capacity of 2479 mAh g^{-1} at 10 mA cm^{-2} and supports extended operation through a modular mechanical recharge strategy over 1000 cycles, corresponding to projected lifetimes exceeding 8000 h. The device maintains structural integrity over 3000 bending cycles at a bending radius of 1 mm and exhibits stable operation under selected mechanical damage condition such as crumpling, cutting, and perforation. When integrated into skin-conformal systems, the H-AAB provides a stable, low-noise power supply for high-fidelity ECG and EMG monitoring, achieving signal fidelities of up to 31.1 dB. These results provide a broadly applicable strategy for designing self-hydrating hydrogel electrolytes in ultrathin aqueous MABs, offering a scalable energy platform for next-generation epidermal bioelectronics.

4 | Materials and Methods

4.1 | Materials

Acrylamide (AAm, >99%, Sigma–Aldrich), N, N′-Methylenebisacrylamide (MBAA, ≥99.5%, Sigma–Aldrich), acrylic acid (AA, 99%, Samchun, Korea), Potassium persulfate (KPS, 98%, Samchun, Korea), lithium chloride (LiCl, 98.2%, Anhydrous, Samchun, Korea), ethanol (EtOH, 99.9%, Duksan, Korea), and (3-Glycidyloxypropyl)trimethoxysilane (Gly-Si, ≥98%, Sigma–Aldrich) were used as purchased. Stainless steel mesh (SS mesh, 316L, diameter: 25 μm) was used as a GDL of air cathodes. Pt/C (20 wt.% Pt on Vulcan XC-72) and Nafion solution (D520) were used as purchased.

4.2 | Synthesis of Ultrathin HHEs

To synthesize the HHEs, AAm and AA were copolymerized via free-radical polymerization in a custom-developed mold (Figure S3). LiCl was dissolved in 6.65 g of water in vials. After fully mixing and cooling the solutions in a water bath, 0.525, 0.105, and 0.175 g of AAm, MBAA, and AA, respectively, were dissolved. Subsequently, a monomer solution was prepared by adding 0.112 g of KPS to the solution above. The mass of LiCl was 0.282, 1.41, 2.82, or 4.23 g, depending on the HHE concentration. The prepared monomer solution was poured into the mold and stored in a 60°C oven for 2 h. The HHEs were cut into the desired size (1.1 cm × 1.1 cm for this study) before use.

4.3 | Fabrication of H-AABs

To fabricate the H-AABs, an air cathode and an Al anode were prepared. First, a Pt/C catalyst ink was prepared. In a vial, 0.1 g of Pt/C powder was added to a 4 g EtOH/H_2O mixture (1:1 by mass), followed by the addition of 0.6 g of Nafion solution. Subsequently, the mixture was sonicated for 1 h to obtain a homogeneous ink. The ink was sonicated for an additional 30 min prior to every use. This catalyst ink was spray coated onto the SS mesh to prepare the air cathode using the ultrasonic spray-casting method. The feed rate was 0.2 mL/min, the air flow rate was 5 L/min, and the frequency was 180 Hz. The SS layer was heated to 90°C on a hot plate. The distance to the nozzle was approximately 4 cm and the mass loading of the catalysts was 1 to 1.2 mg cm^{-2}. A 26-μm-thick Al foil was used as an anode. Gly-Si was used to stabilize the Al anode surface, as described in a previous study [44]. Additionally, 5 wt.% Gly-Si solution in EtOH was prepared and Al foils were stored in the solution for 24 h. Subsequently, excess Gly-Si solution was rinsed with EtOH and cured in a 130°C vacuum oven to fix a Gly-Si coating layer on the Al surface. Finally, H-AABs were fabricated by vertically stacking the Al anode, HHEs, and air cathode. The areal and gravimetric specific capacities of the H-AABs were calculated by normalizing the measured discharge capacity to the active Al anode area and the consumed Al mass, respectively. The consumed Al mass was determined from the mass difference of the Al anode before and after discharge.

$$Q\ \left[mAh\ cm^{-2}\right] = \frac{I \times t}{A}$$

$$Q\ \left[mAh\ g^{-1}\right] = \frac{I \times t}{m_{Al,0} - m_{Al,d}}$$

Where, I (mA) is applied current, t (h) is discharge time, A (cm^2) is the Al anode area, and $m_{Al,\,0}$ and $m_{Al,d}$ (g) are mass of Al before and after discharge, respectively.

4.4 | Characterization

A Raman spectroscope (LabRAM HR Evolution, Horiba) equipped with a confocal microscope (BX41, Olympus) was used to characterize the chemical environment of the water molecules in different HHE concentrations ranging from 400 to 4000 cm^{-1} under a 532 nm light source. The OH stretch peak was deconvoluted using the built-in function of the Origin software. DSC (DSC 200 F3 Maia, Netzsch) was used to characterize the thermal properties of LiCl solutions from −100°C to 60°C at a scan rate of 5°C/min. Electrochemical analyses of the AABs were performed using a potentiostat (CS310X, Corrtest Instruments) for galvanostatic discharge and electrochemical impedance spectroscopy (EIS) was performed in a benchtop climate chamber (LP4006, Shanghai Jianheng Instrument Co., Ltd.). The mechanical flexibility of the H-AABs (2 × 11 cm^2) was evaluated by measuring the bending diameter at the curvature site using vernier calipers during deformation. The mechanical rechargeability of the H-AABs was tested during galvanostatic discharge by replacing the Al anode with a fresh one every cycle. HHEs were also replaced every 20 cycle. Ionic conductivity was determined based on EIS data using the equation σ = (d)/(R × A), where σ represents the ionic conductivity, d the distance between electrodes, R the resistance, and A the electrode area. ITO glasses were used as electrodes on both sides of the HHEs for EIS measurements. The porous structures of freeze-dried HHEs were observed using scanning electron microscopy (SEM, SU8600, Hitachi). The mechanical properties of various HHEs were measured using a universal testing machine (UTM, LDW-5, Jinan Chuanbai Instrument Equipment Co., Ltd.). All specimens for UTM measured 1 cm × 4 cm and 1 mm thick. An anticorrosion test was conducted by contacting the HHEs and Al foil under ambient conditions for 24 h. The mass change of the Al foil (Δm) was measured, whereas the corrosion rate ν (mg cm^{-2} h^{-1}) and anticorrosion efficiency η_H (%) were calculated using the following equations, respectively [45, 46]:

$$\nu = \frac{\Delta m}{24 \times A}$$

$$\eta_H = \frac{\nu_{1m} - \nu}{\nu_{1m}}$$

where A is the surface area of the Al foil, which is 1 cm^2 in this study; and ν_{1m} is the corrosion rate of Al anode on the 1 m HHEs. The diffusion behavior of the HHEs was modeled using Fick's second law to quantify the effective water diffusion coefficient ($D_{\text{diffusion}}$). $D_{\text{diffusion}}$ was calculated using the following equation:

$$\frac{M_t - M_e}{M_0 - M_e} = 1 - \frac{2}{d}\left(\frac{D_{diffusion} \times t}{\pi}\right)^{1/2}$$

where M_t, M_e, and M_0 are the mass of the hydrogel at time t, equilibrium, and initial state in the humid chamber, respectively; and d is the thickness of the HHEs.

4.5 | Real-Time ECG and EMG Signal Recording

The fabrication methods for the OECT-based skin-conformal biosensors are described in the Supporting Information. For ECG signal acquisition, the biosensor was conformally laminated onto the right wrist using a droplet of phosphate-buffered saline to promote ionic coupling and stable skin contact, while a conventional gel electrode was placed on the chest to serve as a reference terminal. The S/N ratio was calculated as the ratio of the peak signal amplitude to the standard deviation

of the baseline current within the quiescent interval between adjacent peaks. For EMG signal measurements, the same electrical configuration was adopted, with both the integrated device and reference gel electrode conformally attached to the wrist to detect localized muscular activity. During the measurements, the participants were instructed to alternately flex (downward) and extend (upward) the wrist to produce direction-dependent muscle contractions of varying intensities. These voluntary motions generated distinct modulations in the drain current, which corresponded to the electrophysiological response of the forearm muscles under different force directions. The recorded EMG waveforms were processed offline to extract the RMS amplitudes using a custom MATLAB script, thus enabling a quantitative assessment of the muscle activation strength.

All the real-time physiological signals were recorded using an integrated device connected to an external Cr/Au (10/45 nm) interconnect line, which was extended to an alligator clip and connected to a gel electrode. The output was routed through an SR570 preamplifier (Stanford Research Systems) and captured using a data-acquisition system at a sampling rate of 1 kHz under zero-bias operation.

Additional Information

All data supporting the findings of this study are available within the Article and its Supplementary Information.

Author Contributions

Jaeil Park: methodology, investigation, writing – original draft, writing – review and editing, visualization, formal analysis, conceptualization, data curation, project administration. **Inho Lee**: data curation, formal analysis, visualization, conceptualization, methodology. **Namhee Kim**: data curation, formal analysis, methodology. **Wonseok Shin**: data curation, formal analysis, methodology. Joo Sung Kim: writing – review and editing. Daegun Kim: writing – review and editing, visualization. **Giwon Lee**: visualization, writing – review and editing. **Jinhan Cho**: visualization, writing – review and editing. **Hoon-Hee Ryu**: visualization, writing – review and editing. **MyungHan Yoon**: visualization, writing – review and editing. Seung Joon Yoo: visualization, writing – review and editing. **Woo-Jin Song**: visualization, writing – review and editing. **Sungjun Park**: supervision, methodology, visualization, writing – review and editing, funding acquisition, resources, conceptualization, project administration, validation, investigation.

Acknowledgements

This study was supported by National Research Foundation of Korea (NRF) grants funded by the Korean government (MSIT) (RS-2025-16903034, RS-2023-00213089, RS-2024-00403639, and RS-2025-25413074). Additional support was provided by the Technology Innovation Program funded by the Ministry of Trade, Industry & Energy (MOTIE, Korea) (Grant No. RS-2022-00154781); the Ministry of Agriculture, Food and Rural Affairs (MAFRA) (Grant No. RS-2026-25503336); the Information Technology Research Center (ITRC) support program funded by MSIT, Korea and supervised by the Institute for Information & Communications Technology Planning & Evaluation (IITP) (Grant No. IITP-2023-2020-0-01461); and a Korea Basic Science Institute (National Research Facilities and Equipment Center) grant funded by the Ministry of Science and ICT (Grant No. RS-2024-00403163).

Conflicts of Interest

The authors declare no conflicts of interest.

Data Availability Statement

The data that support the findings of this study are available from the corresponding author upon reasonable request.

References

1. Y. Mun, S. Park, Y. Kim, et al., "Stretchable and Skin-Conformal Thermoelectric Generator with Highly Flexible and Plastically Bendable Silver Selenide Films," *ACS Applied Materials & Interfaces* 16 (2024): 44841–44849, https://doi.org/10.1021/acsami.4c08741.

2. W. He, P. Li, H. Wang, et al., "Robustly and Intrinsically Stretchable Ionic Gel-Based Moisture-Enabled Power Generator with High Human Body Conformality," *ACS Nano* 18 (2024): 12096–12104, https://doi.org/10.1021/acsnano.3c08543.

3. C. Hwang, J. Hwang, M. J. Kwak, H. S. Kim, H. K. Song, and W. J. Song, "Highly Flexible Electrodes Based on Nano/Micro-Fiber for Flexible Lithium Metal Batteries," *Advanced Functional Materials* 34 (2024): 2404649, https://doi.org/10.1002/adfm.202404649.

4. D. W. Kim, S. W. Kim, G. Lee, et al., "Fabrication of Practical Deformable Displays: Advances and Challenges," *Light: Science & Applications* 12 (2023): 61, https://doi.org/10.1038/s41377-023-01089-3.

5. S. Lee, Y. Lee, W. J. Song, et al., "Integration of Deformable Matrix and Lithiophilic Sites for Stable and Stretchable Lithium Metal Batteries," *Energy Storage Materials* 73 (2024): 103850, https://doi.org/10.1016/j.ensm.2024.103850.

6. L. Zhang, Y. Liu, and X. Huang, "Dynamic Thermal Runaway Evolution of Li-ion Battery during Nail Penetration," *International Journal of Heat and Mass Transfer* 233 (2024): 126020, https://doi.org/10.1016/j.ijheatmasstransfer.2024.126020.

7. N. Mao, S. Gadkari, Z. Wang, T. Zhang, J. Bai, and Q. Cai, "A Comparative Analysis of Lithium-ion Batteries with Different Cathodes under Overheating and Nail Penetration Conditions," *Energy* 278 (2023): 128027, https://doi.org/10.1016/j.energy.2023.128027.

8. L. Ye, M. Liao, K. Zhang, et al., "A Rechargeable Calcium–oxygen Battery That Operates at Room Temperature," *Nature* 626 (2024): 313–318, https://doi.org/10.1038/s41586-023-06949-x.

9. Y. Nam, D. Shin, J. G. Choi, et al., "Ultra-Thin GaAs Single-Junction Solar Cells for Self-Powered Skin-Compatible Electrocardiogram Sensors," *Small Methods* 8 (2024): 2301735, https://doi.org/10.1002/smtd.202301735.

10. M. Mariello, L. Fachechi, F. Guido, and M. C. De Vittorio, "Conformal, Ultra-Thin Skin-Contact-Actuated Hybrid Piezo/Triboelectric Wearable Sensor Based on AlN and Parylene-Encapsulated Elastomeric Blend," *Advanced Functional Materials* 31 (2021): 2101047, https://doi.org/10.1002/adfm.202101047.

11. X. Han, X. Yang, and K. Zhang, "A Conformable and Stretchable Thermoelectric Generator for Efficient Body Heat Harvesting," *ACS Applied Electronic Materials* 6 (2024): 8608–8616, https://doi.org/10.1021/acsaelm.3c01851.

12. D.-Y. Han, C. K. Song, G. Lee, W.-J. Song, and S. Park, "A Comprehensive Review of Battery-Integrated Energy Harvesting Systems," *Advanced Materials Technologies* 9 (2024): 2302236.

13. P. Fan, Z. Zhu, and Q. Hu, "Investigation on Free Relaxation Process Influencing Energy Harvesting Performance of Dielectric Elastomer Generators in Intermittent Motion," *Sensors and Actuators A: Physical* 347 (2022): 113944, https://doi.org/10.1016/j.sna.2022.113944.

14. K. Fan, D. Wei, Y. Zhang, P. Wang, K. Tao, and R. Yang, "A Whirligig-inspired Intermittent-contact Triboelectric Nanogenerator for Efficient Low-frequency Vibration Energy Harvesting," *Nano Energy* 90 (2021): 106576, https://doi.org/10.1016/j.nanoen.2021.106576.

15. W. Li, L. Wan, Y. Lin, et al., "Synchronous Nanogenerator with Intermittent Sliding Friction Self-excitation for Water Wave Energy Harvesting," *Nano Energy* 95 (2022): 106994, https://doi.org/10.1016/j.nanoen.2022.106994.

16. X. Bi, Y. Jiang, R. Chen, et al., "Rechargeable Zinc–Air versus Lithium–Air Battery: from Fundamental Promises toward Technological Potentials," *Advanced Energy Materials* 14 (2024): 2302388, https://doi.org/10.1002/aenm.202302388.

17. X. Chi, M. Li, J. Di, et al., "A Highly Stable and Flexible Zeolite Electrolyte Solid-state Li–air Battery," *Nature* 592 (2021): 551–557, https://doi.org/10.1038/s41586-021-03410-9.

18. J. Wang, L. Wang, R. Pan, and X. Zhou, "Research on the Thermal Runaway Characteristics and Risks of Square Soft Lithium-Ion Batteries Nail Penetration," *Process Safety Progress* 43 (2024): 606–617, https://doi.org/10.1002/prs.12613.

19. A. Agrawal and C. M. Hussain, "Green and Sustainable Metal–air Batteries for Powering Flexible Wearable Electronics: Current Status and Future Prospects," *Sustainable Energy & Fuels* 8 (2024): 4687–4708, https://doi.org/10.1039/D4SE00555D.

20. Y. Wang, W. Pan, H. Y. H. Kwok, H. Zhang, X. Lu, and D. Y. C. Leung, "Liquid-free Al-air Batteries with Paper-based Gel Electrolyte: a Green Energy Technology for Portable Electronics," *Journal of Power Sources* 437 (2019): 226896, https://doi.org/10.1016/j.jpowsour.2019.226896.

21. Y. Zuo, Y. Yu, J. Feng, and C. Zuo, "Ultrathin Al–air Batteries by Reducing the Thickness of Solid Electrolyte Using Aerosol Jet Printing," *Scientific Reports* 12 (2022): 9801, https://doi.org/10.1038/s41598-022-14080-6.

22. C. Zhu, L. Hu, L. Luo, et al., "Enhanced Self-corrosion Inhibition in Al-air Batteries via Anionic Solvent Chemistry Strategy," *Applied Surface Science* 714 (2025): 164391, https://doi.org/10.1016/j.apsusc.2025.164391.

23. T. H. Pham, W.-H. Lee, J.-H. Byun, and J.-G. Kim, "Improving the Performance of Primary Aluminum-air Batteries through Suppressing Water Activity by Hydrogen Bond-rich Glycerol Solvent Additive," *Energy Storage Materials* 55 (2023): 406–416, https://doi.org/10.1016/j.ensm.2022.12.012.

24. C. Zou, L. Chen, Q. Liu, et al., "Flexible Aluminum-Air Battery Based on High-Performance Three-Dimensional Dual-Network PVA/KC/KOH Composite Gel Polymer Electrolyte," *Langmuir* 40 (2024): 9999–10007, https://doi.org/10.1021/acs.langmuir.4c00159.

25. C. You, R. Wu, X. Yuan, et al., "An Inexpensive Electrolyte with Double-site Hydrogen Bonding and a Regulated Zn^{2+} Solvation Structure for Aqueous Zn-ion Batteries Capable of High-rate and Ultra-long Low-temperature Operation," *Energy & Environmental Science* 16 (2023): 5096–5107, https://doi.org/10.1039/D3EE01741A.

26. Q. Xiong and C. Zhi, "Reframing Electrolyte Coordination for Low-temperature Lithium-metal Batteries," *Energy Z* 2 (2026): 200007.

27. C. Deng, X. Xie, J. Han, et al., "A Sieve-Functional and Uniform-Porous Kaolin Layer toward Stable Zinc Metal Anode," *Advanced Functional Materials* 30 (2020): 2000599, https://doi.org/10.1002/adfm.202000599.

28. A. Chen, C. Zhao, J. Gao, et al., "Multifunctional SEI-Like Structure Coating Stabilizing Zn Anodes at a Large Current and Capacity," *Energy & Environmental Science* 16 (2023): 275–284, https://doi.org/10.1039/D2EE02931F.

29. H. Shan, P. Poredos, Z. Chen, et al., "Hygroscopic Salt-embedded Composite Materials for Sorption-based Atmospheric Water Harvesting," *Nature Reviews Materials* 9 (2024): 699–721, https://doi.org/10.1038/s41578-024-00721-x.

30. L. Feng, H. Yang, X. Dong, H. Lei, and D. Chen, "pH-Sensitive Polymeric Particles as Smart Carriers for Rebar Inhibitors Delivery in Alkaline Condition," *Journal of Applied Polymer Science* 135 (2018): 45886, https://doi.org/10.1002/app.45886.

31. C. D. Díaz-Marín, L. Zhang, Z. Lu, M. Alshrah, J. C. Grossman, and E. N. Wang, "Kinetics of Sorption in Hygroscopic Hydrogels," *Nano Letters* 22 (2022): 1100–1107.

32. H. Wang, J. Wang, Z. Jin, et al., "High-performance Flexible Al-air Batteries with Liquid Alloy-activated Anode," *Journal of Power Sources* 566 (2023): 232920, https://doi.org/10.1016/j.jpowsour.2023.232920.

33. L. Chen, B. Li, L. Zhu, et al., "A PVA/LiCl/PEO Interpenetrating Composite Electrolyte with a Three-dimensional Dual-network for all-solid-state Flexible Aluminum–air Batteries," *RSC Advanced* 11 (2021): 39476–39483.

34. L. Ďuriška, I. Černičková, P. Priputen, and M. Palcut, "Aqueous Corrosion of Aluminum-Transition Metal Alloys Composed of Structurally Complex Phases: a Review," *Materials* 14 (2021): 5418.

35. T. Wang, Z. Tian, Z. You, et al., "Hydrogen-bond Network Manipulation of Aqueous Electrolytes with High-donor Solvent Additives for Al-air Batteries," *Energy Storage Materials* 45 (2022): 24–32, https://doi.org/10.1016/j.ensm.2021.11.030.

36. L. Suo, O. Borodin, T. Gao, et al., "Water-in-salt″ Electrolyte Enables High-voltage Aqueous Lithium-ion Chemistries," *Science* 350 (2015): 938–943, https://doi.org/10.1126/science.aab1595.

37. J. Park, J. Kim, S. Lee, et al., "Unraveling Concentration-dependent Solvation Structures and Molecular Interactions in Water-in-salt Electrolytes for Enhanced Performance of Electric Double-layer Capacitors," *Energy Storage Materials* 65 (2024): 103137, https://doi.org/10.1016/j.ensm.2023.103137.

38. M. Ahmed, V. Namboodiri, A. K. Singh, J. A. Mondal, and S. K. Sarkar, "How Ions Affect the Structure of Water: a Combined Raman Spectroscopy and Multivariate Curve Resolution Study," *The Journal of Physical Chemistry B* 117 (2013): 16479–16485, https://doi.org/10.1021/jp4100697.

39. Q. Hu, H. Zhao, and S. Ouyang, "Understanding Water Structure from Raman Spectra of Isotopic Substitution H_2O/D_2 O up to 573 K," *Physical Chemistry Chemical Physics* 19 (2017): 21540–21547, https://doi.org/10.1039/C7CP02065A.

40. J. Lu, J. Yan, F. Pei, et al., "Shrinkage-Resistant Thermo-Responsive Hygroscopic Hydrogel toward Ultra-Rapid Cycling Atmospheric Water Harvesting," *Advanced Functional Materials* 35 (2025): 2505359, https://doi.org/10.1002/adfm.202505359.

41. G. Graeber, C. D. Díaz-Marín, L. C. Gaugler, et al., "Extreme Water Uptake of Hygroscopic Hydrogels through Maximized Swelling-Induced Salt Loading," *Advanced Materials* 36 (2024): 2211783, https://doi.org/10.1002/adma.202211783.

42. C. Norioka, Y. Inamoto, C. Hajime, A. Kawamura, and T. Miyata, "A Universal Method to Easily Design Tough and Stretchable Hydrogels," *NPG Asia Materials* 13 (2021): 34, https://doi.org/10.1038/s41427-021-00302-2.

43. Y. Yue, "Designing Ultrahigh-Water-Content, Tough, and Crack-Resistant Hydrogels by Balancing Chemical Cross-Linking and Physical Entanglement," *ACS Applied Engineering Materials* 2 (2024): 638–648, https://doi.org/10.1021/acsaenm.3c00726.

44. J. Demopoulos, "Corrosion Resistance of Silane Coatings on Aluminum and Magnesium Alloys," *Honors Research Projects* 551 (2017), https://ideaexchange.uakron.edu/honors_research_projects/551.

45. P. Wu, Q. Zhao, H. Yu, et al., "Modification on Water Electrochemical Environment for Durable Al-Air Battery: Achieved by a Low-Cost Sucrose Additive," *Chemical Engineering Journal* 438 (2022): 135538, https://doi.org/10.1016/j.cej.2022.135538.

46. M. Wei, K. Wang, Y. Zuo, et al., "A Prussian-Blue Bifunctional Interface Membrane for Enhanced Flexible Al–Air Batteries," *Advanced Functional Materials* 33 (2023): 2302243, https://doi.org/10.1002/adfm.202302243.

Supporting Information

Additional supporting information can be found online in the Supporting Information section.

Supporting File: aenm71309-sup-0001-SuppMat.docx.